

# The Surface PSD and Image Degradation due to Mid-Spatial-Frequency Errors

James E. Harvey

Photon Engineering, LLC  
310 S. Williams Blvd., Suite 222  
Tucson, Arizona 86711

## Abstract

In the design and specification of precision optical components for advanced imaging applications it is necessary that residual optical fabrication errors be specified and measured over the “entire range of relevant spatial frequencies”. This includes the mid-spatial-frequency surface errors that span the gap between the traditional “figure” and “finish” errors. Since surface scatter is merely a diffraction phenomenon, the linear systems formulation of non-paraxial scalar diffraction theory forms the basis of the GHS surface scatter theory: a linear systems formulation of surface scatter theory valid for smooth or rough surfaces, large or small incident and scattered angles and arbitrary surface PSDs. The resulting surface transfer function can be combined with the conventional OTF which then characterizes image degradation due to diffraction effects, geometrical aberrations, and *surface scatter effects*. The method of determining the composite surface PSD from the metrology data and the method of predicting the bidirectional scattered distribution function (BSDF) from the surface PSD will be discussed as will the process for deriving the optical fabrication tolerances necessary for satisfying specific image quality requirements.

**Keywords:** Image Analysis, Diffraction, Optical Fabrication, Surface Scattering, BSDF, Modulation Transfer Function.

## 1.0 Introduction

The succession of steps required to calculate image degradation from surface metrology data as promised in the abstract of this paper includes: 1.) determining the composite surface PSD from metrology data over the entire range of relevant spatial frequencies (including the mid-spatial-frequencies that span the gap between the traditional “figure” and “finish” surface errors), 2.) predict the extended BRDF utilizing the GHS surface scatter theory, 3.) discuss Peterson’s analytic expressions for in-field stray radiation for multi-element imaging systems and 4.) apply conventional linear systems theory to calculate the resulting systems modulation transfer function (MTF). These steps are illustrated in Figure 1, and will serve as the subheadings in this paper.

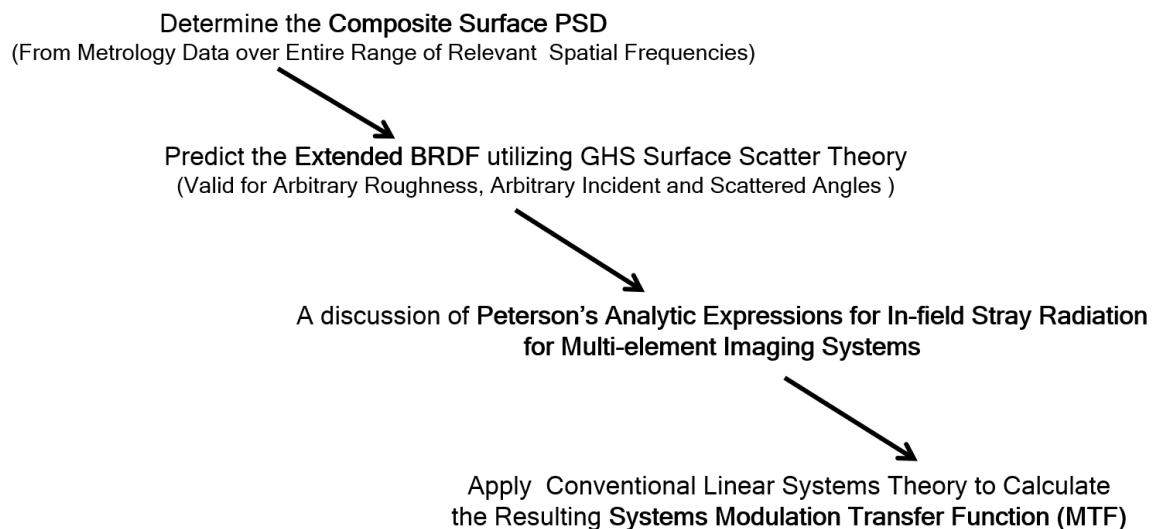


Figure 1. Graphical illustration of the succession of four steps required to calculate image degradation as promised in the abstract.

## 2.0 Determine the Composite Surface Power Spectral Density (PSD) Function

The behavior of light scattered from randomly rough surfaces is dictated by the statistical surface characteristics shown in Figure 2. Note the surface height distribution with the root-mean-square roughness  $\sigma_s$  indicated, and the surface autocovariance (ACV) function labeled  $C(x,y)$  with autocovariance length  $\ell$ , defined as the width of the function at the  $1/e$  height.<sup>1-3</sup>

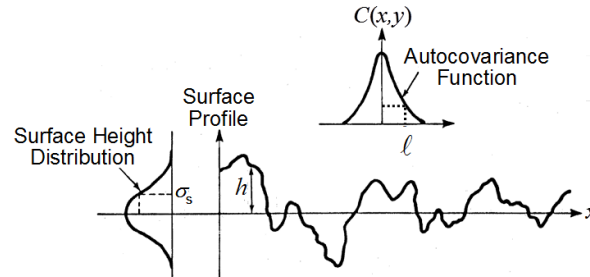


Figure 2. Statistical surface characteristics.

Figure 3 shows the relationship between the surface profile, the surface autocovariance function and the surface power spectral density (PSD) function. Note that the surface ACV and the surface PSD functions are Fourier transforms of each other.

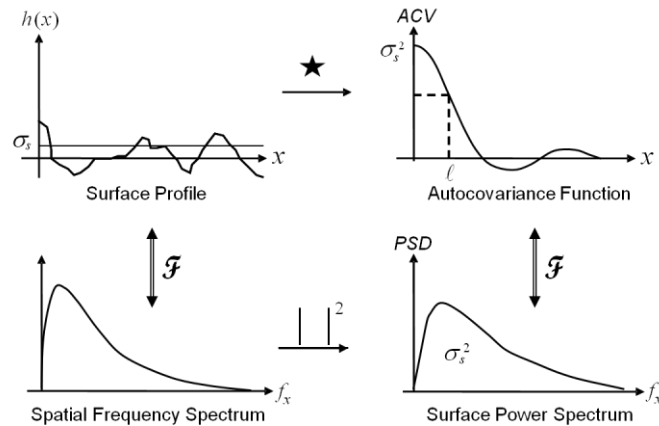


Figure 3. Illustration of the relationship between the surface profile, surface ACV function and the surface PSD function. The ACV and the PSD functions form a Fourier transform pair.

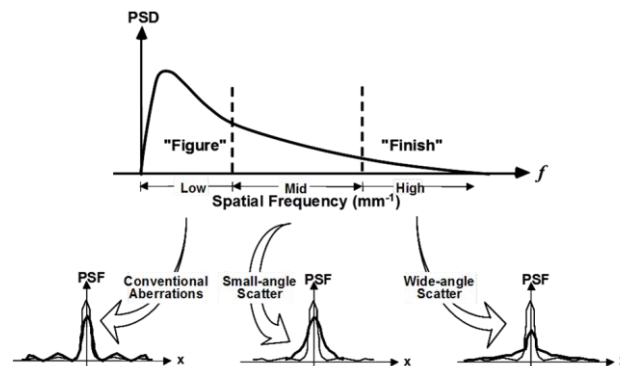


Figure 4. Illustration of different spatial regimes and their resulting effect upon image quality.

Figure 4 shows the surface PSD divided into several different spatial frequency regimes which have distinctly different effects upon image quality. Low spatial frequency figure errors give rise to conventional wavefront aberrations. High spatial frequency microroughness produces a wide-angle scatter halo around the

image core which reduces image contrast without significantly affecting the width of the image core. And the mid-spatial frequency figure errors produce small-angle scatter that broadens the image core, thus reducing resolution.<sup>4</sup>

In 1987 I presented a paper at an X-ray Astronomy Conference at the Annual SPIE Symposium in San Diego in which I stated, “. . . small angle scatter due to mid-spatial-frequency surface ripple is a dominant source of image degradation for many grazing incidence optical systems”.<sup>5</sup>

The session chairman was Stu Bowyer from Berkeley, and his group had designed and built The EUVE Telescope, a grazing incidence Wolter Type II design that had been diamond-turned and post-polished. It had been recently launched and was sending back good data. He stood up and said, “At Berkley, we don’t have mid-spatial-frequency surface errors. That’s a Perkin-Elmer problem.”

Bernt Aschenbach, a noted astrophysicist who had been involved with the European ROSAT X-ray Telescope which was performing superbly, stood up and stated, “In Europe, we don’t have mid-spatial-frequency surface errors either.” He then shook his finger in my face and stated, “that is a United States problem”.

Although Aikens was making extensive use of surface PSD’s for characterizing optical surfaces,<sup>6</sup> and Harvey was specifically discussing mid-spatial-frequencies that span the gap between “figure” errors and “finish” errors,<sup>7-8</sup> it was 21 years later, at the 2008 OSA Topical Meeting on Optical Fabrication and Testing in Rochester, New York that a half-day technical session was finally devoted to the topic of *Specifying and Measuring Mid-Spatial-Frequency Optical Fabrication Errors*.<sup>9-11</sup>

Historically, only low spatial frequency “figure” errors and high spatial frequency “finish” errors had been characterized and specified in the manufacture of optical components. However, it would clearly be a non-physical situation to have significant figure errors and significant finish errors and to have no mid spatial frequency irregularities as shown in Figure 5.

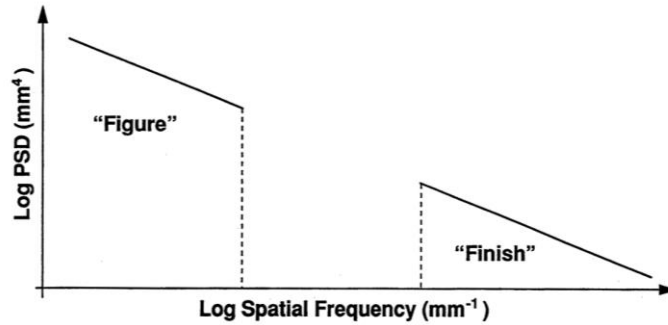


Figure 5. This illustration of a surface PSD that exhibits both low and high-spatial-frequency errors but no mid-spatial-frequency surface errors represents a very non-physical situation!

We all have “mid” spatial frequency surface errors, whether we are aware of them or not. Just because we don’t spec them or measure them doesn’t mean that they are not present and degrading our images.

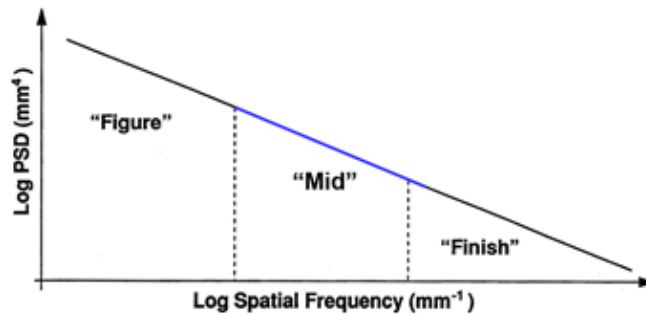


Figure 6. This illustration of a surface PSD with mid-spatial-frequency surface errors spanning the gap between the low and high-spatial-frequency errors represents a much more physically realistic situation!

In fact, we may even have quasi-periodic surface errors that fall into the “mid” spatial frequency domain, resulting in a substantial band-limited “hump” in the surface PSD as shown in Figure 7. This can cause serious degradation of image quality. The Perkin-Elmer Corporation discovered this the hard way when they had to stop fabrication and invent a suitable mid-spatial-frequency interferometer during the AXAF Program.<sup>12</sup> Their computer-controlled figuring was resulting in residual mid-spatial-frequency optical fabrication errors that had not been anticipated, and for which no suitable metrology instrument currently existed.

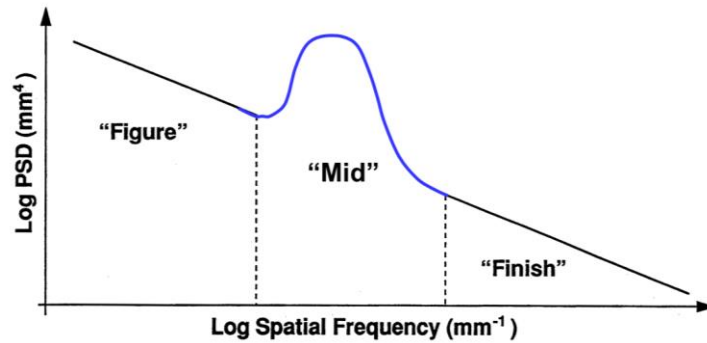


Figure 7. Illustration of a surface PSD exhibiting a large hump in the mid-spatial-frequency range due to the presence of quasi-periodic surface errors falling into that spatial frequency domain.

Incidentally, Eugene Church had discussed the inverse power law, or fractal behavior, of PSD’s of optical surfaces fabricated by conventional grinding and polishing techniques on ordinary glassy materials as early as the late 1970s.<sup>13</sup> And Livermore experimentally showed the inverse power law behavior of the surface PSD of high-quality EUV surfaces over a large dynamic range of spatial frequencies as shown in Figure 8.

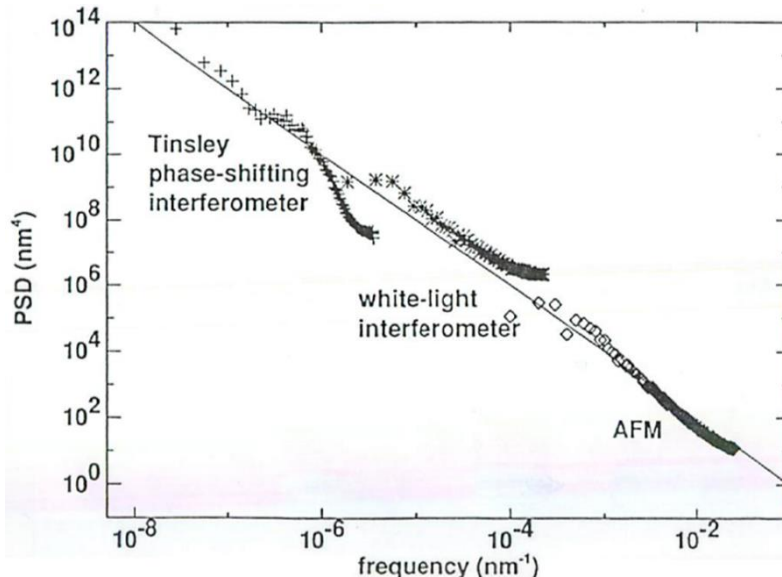


Figure 8. Surface Characteristics of Optics for EUV Lithography.<sup>14</sup>

It often takes three, or even four different metrology instruments to measure the surface characteristics over the entire range of relevant spatial frequencies for a given application. Figure 9. shows the metrology data from the Tinsley EUV mirror built for the NOAA UltraViolet Imager (SUVI) as part of the GOES weather satellite.<sup>15</sup> The low spatial frequency surface errors were measured with a full-aperture interferometer, the high spatial frequency microroughness was measured with an atomic force microscope, and a micro-phase measuring interferometer (with both a 2.5X and a 50X objective) was used to measure the mid spatial frequency surface fabrication errors. Like most optical surfaces fabricated with conventional grinding and polishing

techniques on ordinary glassy materials, the surface PSD exhibits an inverse power law, or fractal, behavior. Following Church and Takas recommendations in Reference 16, we fit an ABC or K-correlation function of the form of Eq. 1 to this metrology data as shown by the heavy red line on Figure 9.

$$PSD(f_x)_{1-D} = \frac{A}{[1 + (B f_x)^2]^{C/2}} \quad (1)$$

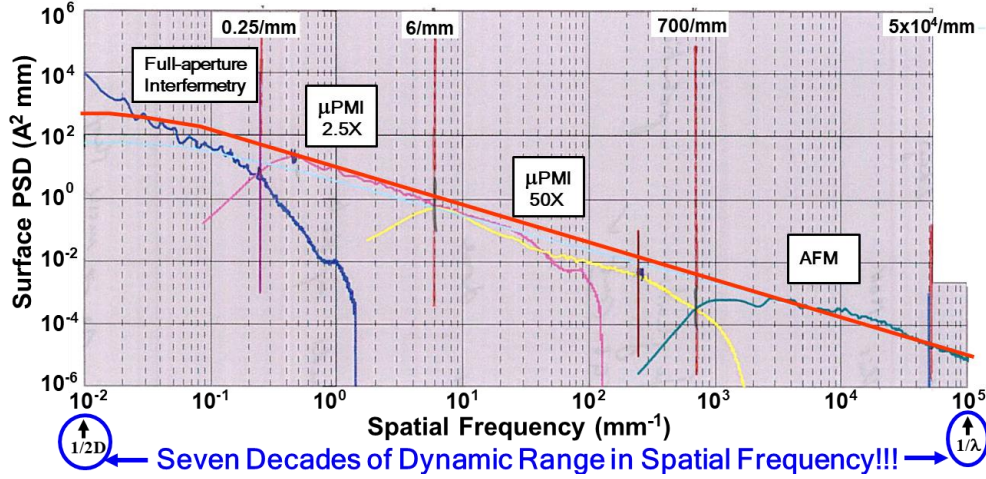


Figure 9. Measured surface PSD fit with an ABC or K-correlation function. Note the large dynamic range of spatial frequencies spanning from the lowest relevant spatial frequency of  $1/2D$  to the highest relevant spatial frequency of  $1/\lambda$ .

The ABC, or K-correlation function expressed by Eq.(1) has several very useful properties. The 2-D surface PSD (assuming isotropic roughness) can be obtained from the 1-D surface profile measurements by using Eq.(2).

$$PSD(f)_{2-D} = K \frac{AB}{[1 + (B f)^2]^{(C+1)/2}}, \quad K = \frac{1}{2\sqrt{\pi}} \frac{\Gamma((C+1)/2)}{\Gamma(C/2)} \quad \begin{array}{l} \text{2-D surface PSD.} \\ f = \sqrt{f_x^2 + f_y^2} \end{array} \quad (2)$$

The total integral under the 2-D surface PSD is given by Eq.(3), and the Fourier transform of the 2-D surface PSD is given by Eq.(4).

$$\sigma_{Total}^2 = \frac{2\pi K A}{(C-1)B} \quad \text{Total integral over the 2-D surface PSD.} \quad (3)$$

$$ACV_s(r) = \sqrt{2\pi} \frac{A}{B} \frac{2^{-C/2}}{\Gamma(C/2)} \left(\frac{2\pi r}{B}\right)^{(C-1)/2} \mathcal{K}_{(C-1)/2}\left(\frac{2\pi r}{B}\right) \quad (4)$$

where  $\mathcal{K}_{(C-1)/2}$  is the modified Bessel function of the 2<sup>nd</sup> kind and  $r = \sqrt{x^2 + y^2}$ .

We must also replace the total or intrinsic roughness,  $\sigma_s$ , with the bandlimited *relevant rms roughness*  $\sigma_{rel}$  in the classical expression for *total integrated scatter*, TIS.<sup>17</sup>

$$TIS = 1 - \exp[-(4\pi \cos \theta_i (\sigma_{rel} / \lambda)^2)] \quad (5)$$

The total intrinsic roughness,  $\sigma_s$ , of any surface is defined as the square root of the (infinite) integral of the surface PSD.

$$\sigma_s^2 = \int_{f_x=-\infty}^{\infty} \int_{f_y=-\infty}^{\infty} S_2(f_x, f_y) df_x df_y \quad (6)$$

It is important to recognize that the relevant (or effective) surface roughness is not an intrinsic surface characteristic, but a band-limited quantity that depends upon the wavelength and incident angle.<sup>17</sup>

Any portion of the surface PSD that extends outside of the circle of radius  $1/\lambda$  centered upon a spatial frequency of  $f_o = \sin\theta_o/\lambda$  will not scatter light; i.e., it is irrelevant roughness with respect to surface scatter phenomena. For isotropic roughness and normal incidence, Eq.(7) mathematically defines and Figure 10 (a) graphically illustrates the relevant roughness. For isotropic roughness and non-normal incidence, Eq.(8) mathematically defines and Figure 10 (b) and (c) graphically illustrates the relevant roughness.<sup>17</sup>

$$\sigma_{rel}^2(\lambda) = 2\pi \int_{f=0}^{1/\lambda} S_2(f) f df \quad (7)$$

$$\sigma_{rel}^2(\lambda, \theta_i) = \int_{-1/\lambda+f_o}^{1/\lambda+f_o} \int_{-\sqrt{1/\lambda^2-(f_x-f_o)^2}}^{+\sqrt{1/\lambda^2-(f_x-f_o)^2}} S_2(f_x, f_y) df_x df_y \quad (8)$$

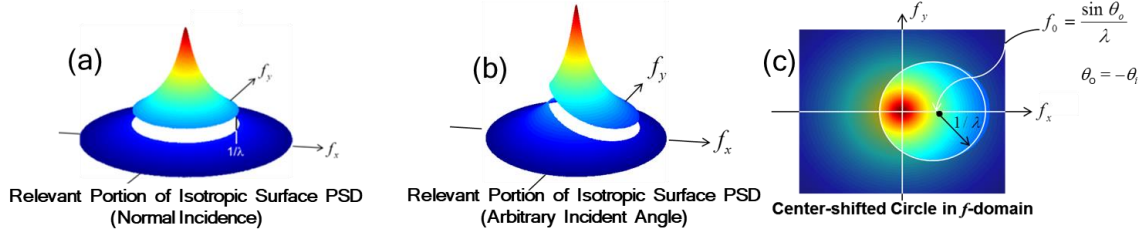


Figure 10. Graphical illustration of the relevant roughness for: (a) isotropic roughness and normal incidence, (b) and (c) isotropic roughness and non-normal incidence.<sup>17</sup>

### 3.0 Predict Extended BRDF Utilizing the GHS Surface Scatter Theory.

The GHS surface scatter theory, a linear systems formulation valid for arbitrary surface roughness, arbitrary incident and scattered angles and arbitrary surface PSD functions is summarized by Eq.(9), which is a mathematical expression for the *surface transfer function*.<sup>18-19</sup> The  $C(\hat{x}, \hat{y})$  in is merely the surface ACV function provided by Eq(4). Eq(10) indicates that the BSDF of the surface is then given by multiplying the Fourier transform of this surface transfer function by the polarization reflectance,  $Q$ .<sup>18-19</sup>

$$H_s(\hat{x}, \hat{y}; \gamma_i, \gamma_s) = \exp \left\{ -[2\pi \hat{\sigma}_{rel}(\gamma_i + \gamma_s)]^2 [1 - C_s(\hat{x}, \hat{y})/\sigma_s^2] \right\} \quad (9)$$

$$BRDF = Q \mathcal{F} \{ H(\hat{x}, \hat{y}; \gamma_i, \gamma_s) \}, \quad Q = \text{Polarization Reflectance} \quad (10)$$

Note that a scaled coordinate system has been used in which the spatial variables are normalized by the wavelength of the light ( $\hat{x} = x/\lambda$ ,  $\hat{y} = y/\lambda$ , etc.). The reciprocal variables  $\alpha$ ,  $\beta$  and  $\gamma$  are thus the *direction cosines* of the propagation vectors of the angular spectrum of plane waves discussed by Ratcliff,<sup>20</sup> Goodman,<sup>21</sup> and Gaskill.<sup>22</sup> Also, don't be fooled by the fact that we have reduced the GHS theory into a single mathematical expression. Upon close inspection of Eq(9), we see that it is really an expression for a two-parameter family of surface transfer functions; i.e,  $H_s$  is a function of two independent variables,  $\hat{x}$  and  $\hat{y}$ , and two additional parameters,  $\gamma_i$  and  $\gamma_s$ , which are equal to  $\cos(\theta_i)$  and  $\cos(\theta_s)$ . In other words, the GHS theory is no longer shift-invariant. It requires a different surface transfer function for each incident and scattering angle!<sup>18-19</sup>

We thus have to calculate the BSDF *one point at a time* by choosing an incident and a scattering angle, then implementing a 2D *FFT* numerical Fourier transform algorithm indicated symbolically by the script  $\mathcal{F}$  in Eq.(10). Furthermore, due to the large dynamic range in spatial frequency, we have to utilize an *FFTLog* Fourier transform algorithm<sup>23</sup> to reduce the time and memory requirements in actually performing the computations indicated in Eq(10).

This computationally intensive process is quite manageable for surfaces with isotropic roughness and has been quantitatively compared to the classical small perturbation method (Rayleigh-Rice), the Kirchhoff approximation method, and the rigorous method of moments for surfaces with both Gaussian and inverse power law surface PSDs.<sup>24</sup>

Figure 11 illustrates BSDF profiles predicted for six EUV wavelengths and two visible wavelengths from the SUVI mirror metrology data previously shown in Figure 9. Note from the embedded Table that the TIS

for the smallest EUV wavelength exceeded 56%! The two visible wavelengths allowed us to compare our GHS predictions with classical Rayleigh-Rice computations for smooth surfaces.<sup>25-26</sup>

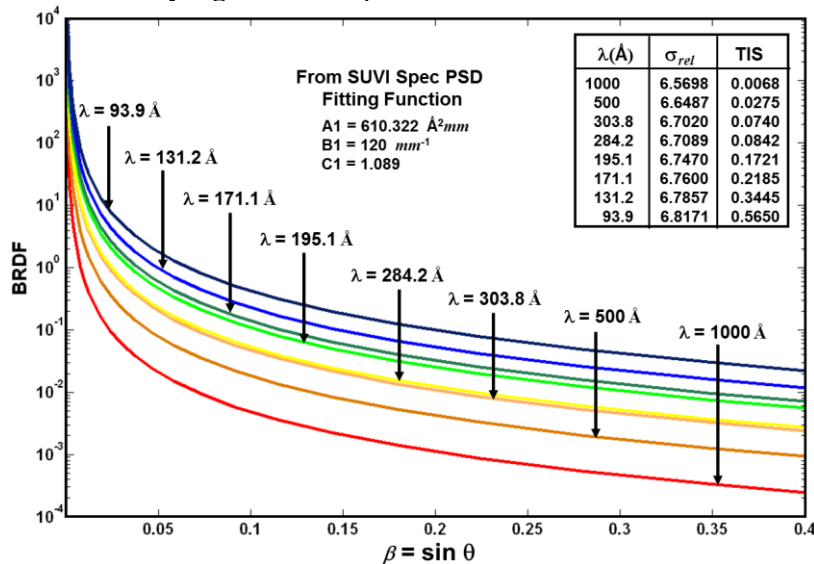


Figure 11. These BSDF profiles were numerically calculated from the real metrology data (surface PSD) illustrated in Figure 9. The GHS surface scatter theory was used for this moderately rough surface. The FFTLog algorithm was implemented in the calculations.

#### 4.0 Peterson’s Analytical Model for Stray Light from Multi-element Imaging Systems.

So far, we have only discussed scattering from a single optical surface. This 3<sup>rd</sup> step is a discussion of Peterson’s Analytic Model for Stray Light from *Multi-element Imaging Systems*.<sup>27</sup> We first describe Peterson’s analytical model, then, since Peterson had a smooth-surface assumption in his model that allowed him to ignore the multi-scattered light, we generalized his model so it could be used for our EUV applications. Finally, we applied it to a two-mirror EUV telescope.

In the more extensive version of Reference 27 that served as a Master’s Report at the Optical Sciences Center at the University of Arizona, Peterson emphasized that:

- (1) Although optical systems are complex, the distribution of scattered light from their elements is not.
- (2) The halo of scattered light that surrounds a bright source image is merely the sum of the contributions from each element.
- (3) Furthermore, the scattered-light irradiance distribution from any one element has the form of that element’s BSDF, and its magnitude and scale depend only on the size of the beam that passes through that element.

Making use of the Lagrange invariant of 1st-order imaging theory and the brightness theorem (conservation of radiance), the scattered irradiance in the focal plane of an imaging system from the  $j$ th element for an in-field point source has been shown by Peterson to be given by<sup>27</sup>

$$E_{sj}(r) = E_{ent} \pi (na)^2 T \frac{s_{ent}^2}{s_j^2} BSDF \left( (na) \frac{r}{s_j} \right) \quad (11)$$

where **BSDF** is the bi-directional scatter distribution function,  $r$  is the radial distance from the point source geometrical image in the image plane of the telescope,  $na$  is the numerical aperture of the system,  $T$  is the system transmittance,  $s_{ent}$  is the radius of the entrance pupil,  $s_j$  is the radius of the beam on the  $j$ th element, and  $E_{ent}$  is the irradiance in the entrance pupil of the system. This formulation is based upon both a smooth-surface and a paraxial assumption. For a two-mirror telescope, we can thus write<sup>27</sup>

$$E_s(r) = E_{ent} \pi (na)^2 T s_{ent}^2 \left[ \frac{BSDF_p((na) r / s_p)}{s_p^2} + \frac{BSDF_s((na) r / s_s)}{s_s^2} \right] \quad (12)$$

Since  $s_{ent} = s_p$ ,  $na = 1/(2F^\#) = s_p/f'$  ( $f'$  = system focal length) and the total power reaching the focal plane is given by,  $P_T = E_{ent} \pi s_p^2 T$ , the scattered irradiance in the telescope focal plane normalized by the total power is given by<sup>27</sup>

$$\frac{E_s(r)}{P_T} = \left( \frac{1}{f'} \right)^2 \left[ BSDF_p(r/f') + \left( \frac{s_p}{s_s} \right)^2 BSDF_s((s_p/s_s)(r/f')) \right] \quad (13)$$

And if there were more scattering surfaces in the imaging system, there would be additional BSDF terms added in the square bracket of Eq.(13).

For a two-mirror telescope the point spread function (PSF) in the focal plane of the telescope will consist of the sum of four components whose radiant power distribution is listed below<sup>26</sup>

$$\text{Direct-direct component (Specular): } P_{dd}/P_T = A_p A_s \quad (1)$$

$$\text{Scattered-direct component: } P_{sd}/P_T = B_p A_s \quad (2)$$

$$\text{Direct-scattered component: } P_{ds}/P_T = A_p B_s \quad (3)$$

$$\text{Scattered-scattered component: } P_{ss}/P_T = B_p B_s \quad (4)$$

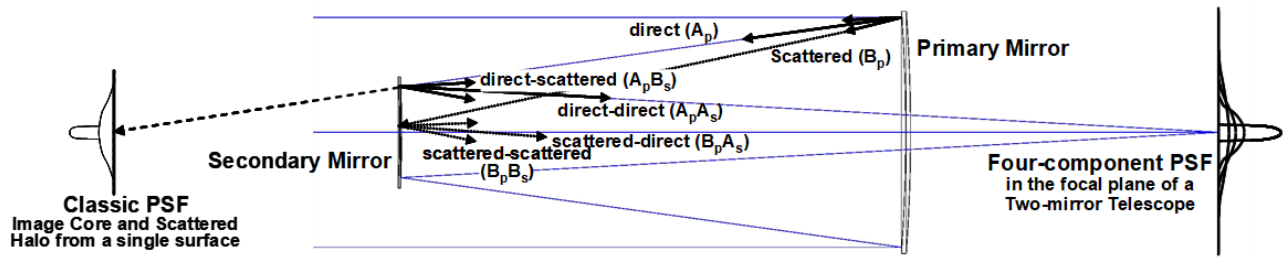


Figure 12. Illustration of the four components making up the PSF of a two-mirror telescope.<sup>26</sup>

Assuming isotropic roughness on both the primary and secondary mirrors, we can construct the following expression for the telescope PSF

$$PSF(r) = PSF_{dd}(r) + PSF_{sd}(r) + PSF_{ds}(r) + PSF_{ss}(r) \quad (14)$$

The first term of the PSF is the image core, or specular beam, as determined by diffraction and geometrical aberrations. And the two middle terms are determined by Peterson's analytical expressions. Peterson ignored the 4<sup>th</sup> term due to his smooth-surface assumption.

The fraction of the total reflected radiant power remaining in the specular beam after reflection from a single moderately rough surface is given by<sup>25-26</sup>

$$A = \exp[-(4\pi \cos \theta_i \sigma_{rel}/\lambda)^2] \quad (15)$$

and the fraction of the total reflected radiant power contained in the scattered halo, or total integrated scattering (TIS), is given by<sup>25-26</sup>

$$B = \text{TIS} = 1 - A = 1 - \exp[-(4\pi \cos \theta_i \sigma_{rel}/\lambda)^2], \quad (16)$$

where  $\theta_i$  is the angle of incidence and  $\sigma_{rel}$  is the rms surface roughness measured over the entire range of relevant spatial frequencies (spatial frequencies greater than  $1/\lambda$  are irrelevant since, they do not contribute to the scattered radiation).<sup>25-26</sup>

The quantities  $A_p$ ,  $B_p$ ,  $A_s$  and  $B_s$  are determined from Eq.(15) and Eq.(16). Figure 13 graphically illustrates the radiant power distribution among these four components of the PSF of a two-mirror telescope (same BSDF from both mirrors) as a function of the rms roughness of the mirrors expressed in wavelength ( $\sigma/\lambda$ ).

Note that the TIS of the two-mirror telescope is equal to  $1-A_pA_s$ . It is evident from Figure 13 that for  $\sigma/\lambda < 0.02$  scattering effects are modest, with a TIS  $< 0.12$ . However, as  $\sigma/\lambda$  increases, the scattered light increases rapidly. At  $\sigma/\lambda = 0.066$  each of the four components contain 25% of the total power. As  $\sigma/\lambda$  continues to increase, the power in the scattered-scattered component increases and the power in all other components decreases. For  $\sigma/\lambda > 0.12$  the specular beam has essentially vanished, and for  $\sigma/\lambda > 0.18$  virtually all the radiant power is in the scattered-scattered component.

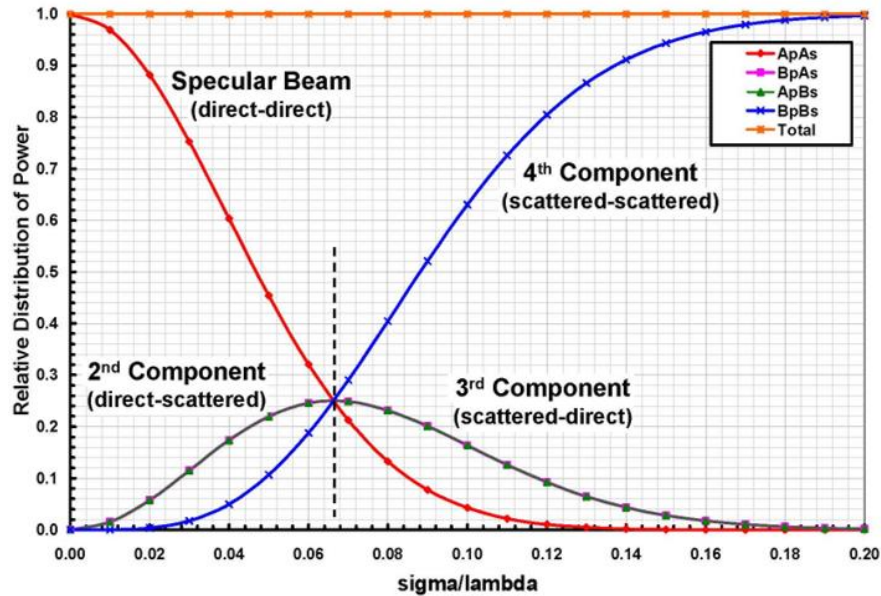


Figure 13. Energy distribution among the four PSF components.<sup>26</sup>

For some short-wavelength application, such as solar EUV telescopes, surface scattering from state-of-the-art primary and secondary mirrors will dominate both geometrical aberrations and diffraction effects in the degradation of image quality.

As discussed above, we know the fraction of the total radiant power contained in the scattered-scattered beam. But what is the angular distribution of radiation in the scattered-scattered beam?

Let us think of the scattering process as one whereby each geometrically traced ray, on reflection from a mirror surface, spawns a multitude of scattered rays randomly distributed and weighted according to the mirror's BSDF. These scattered rays are then traced through the system, each one spawning another distribution of scattered-scattered rays when it encounters another mirror surface. Each new family of scattered rays will be randomly distributed and weighted according to the second mirror's BSDF. This is precisely the description of a convolution operation.

We thus generalize the Peterson analytical treatment (i.e.; removed the smooth-surface limitation) by accurately calculating and adding the effects of the scattered-scattered component to the PSF in the focal plane of the telescope. The functional form of the scattered-scattered term of Eq.(14) is obtained by convolving the two middle terms, which is done by numerically calculating the Hankel transform of the product of the Hankel transforms of the BSDF's provided for the two mirrors. Finally, care is taken to properly normalize the magnitude of each component of the PSF.<sup>26</sup>

This generalized Peterson analytical technique was then used to predict the image quality of a two-mirror Ritchey-Chretien EUV solar telescope. This provided insight and understanding concerning the surface scatter effects upon telescope image quality that is difficult to obtain with brute-force computational approaches.

The Figure 14 shows a direct comparison of the irradiance in the focal plane as predicted by the generalized Peterson analytical method with predictions from scattering calculations from both the ZEMAX and ASAP optical analysis codes.<sup>26</sup>

The three approaches are in excellent agreement, even for the shortest wavelength of interest that does not satisfy the smooth-surface approximation.

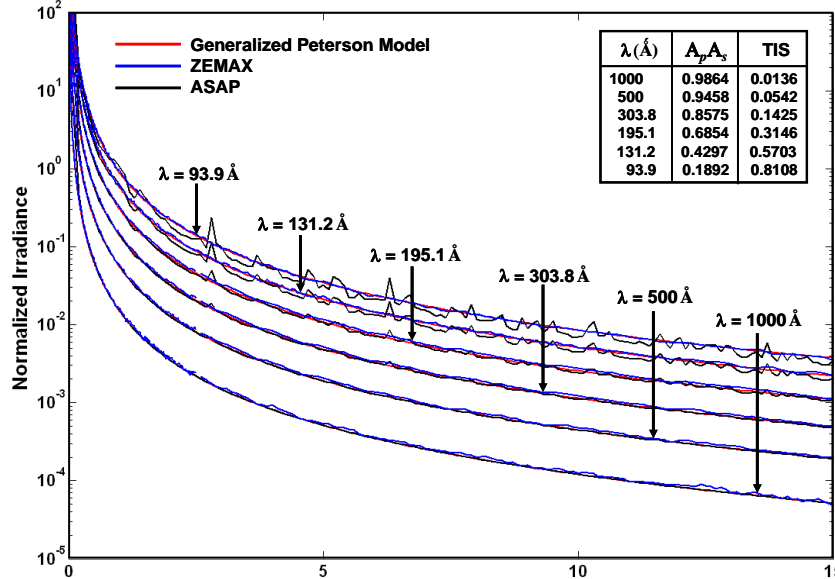


Figure 14. Radial distances from Gaussian image point (mm).<sup>26</sup>

### 5.0 Apply Linear Systems Theory to Calculate System MTF (including surface scatter effects).

Linear systems theory tells us that if image degradation mechanisms are independent and uncorrelated, the system transfer function is given by the product of the transfer functions of the separate image degradation mechanisms. From the convolution theorem of Fourier transform theory, the system PSF will thus be given by the convolution of the separate PSFs.

$$\begin{aligned}
 & \text{Classical MTF} \\
 H_{\text{system}} &= (H_{\text{diffraction}} H_{\text{aberrations}}) H_{\text{scattering}} \\
 & \updownarrow \mathcal{F} \qquad \qquad \updownarrow \mathcal{F} \\
 PSF_{\text{sys}} &= PSF_{\text{diff}} * PSF_{\text{aberr}} * PSF_{\text{scat}}
 \end{aligned} \tag{17}$$

The product of the classical MTF with the surface transfer function (due to residual optical fabrication errors) will thus comprise the system, or composite, MTF in the presence of surface scatter. The rest of this discussion draws extensively from Reference 28.

Assuming an imaging system with a circular aperture ( $D = 50\text{mm}$ ,  $f = 200\text{mm}$ ) operating at a wavelength of  $\lambda = 0.5\mu\text{m}$ , the diffraction-limited MTF is given by<sup>29</sup>

$$MTF = \frac{(D^2 / 2) \{ \cos^{-1}(r/D) - (r/D)[1 - (r/D)^2]^{1/2} \}}{\pi D^2 / 4} \tag{18}$$

and has a cut-off spatial frequency  $\xi_c = D / \lambda f = 500\text{mm}^{-1}$  as shown in Figure 15.

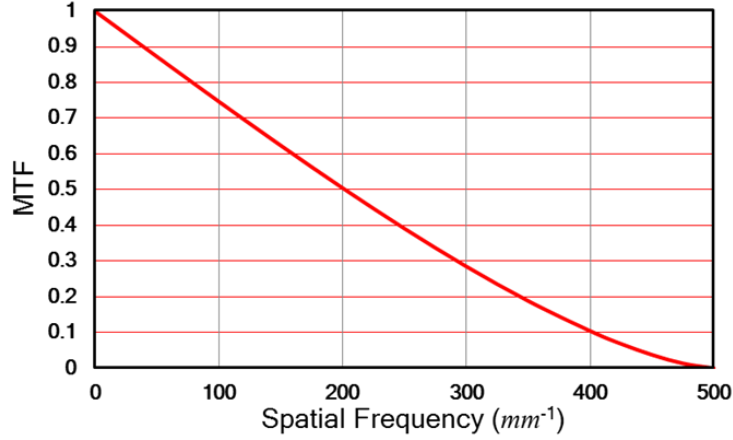


Figure 15: Diffraction-limited MTF of imaging system with a circular aperture.

Assume also that there is a single reflecting surface with a Gaussian ACV function that produces a TIS = 0.2 (corresponds to an rms roughness of  $\sigma = 188\text{\AA}$ )

$$ACV_{2D}(\hat{r}) = C_s(\hat{x}, \hat{y}) = \sigma^2 \text{Gauss} \left\{ \frac{\hat{r}}{\ell} \right\} = \sigma^2 \exp \left[ -\pi \left( \frac{\hat{r}}{\ell} \right)^2 \right], \quad \ell = 2.0 \text{ mm} . \quad (19)$$

For smooth surfaces, the STF is given by

$$STF = A + BG(\hat{x}, \hat{y}) \approx A + B C_s(\hat{x}, \hat{y}) / \sigma^2 \quad (20)$$

$$STF \approx 0.8 + 0.2 \text{ Gauss} \left\{ \frac{\hat{r}}{\ell} \right\} \Big|_{r=\rho\lambda f} = 0.8 + 0.2 \exp \left\{ -\pi \left( \frac{\rho}{\ell/\lambda f} \right)^2 \right\} \quad (21)$$

and illustrated graphically in Figure 16. We have increased the surface correlation width substantially beyond what it would typically be to enable seeing the nature of the STF at small spatial frequencies.

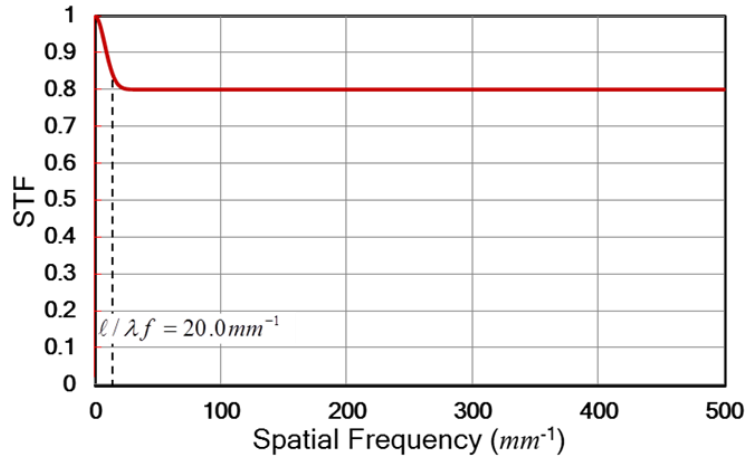


Figure 16: Surface transfer function for above example.

The system transfer function is given by the product of the classical MTF and the STF

$$H(\hat{x}, \hat{y})_{\text{sys}} = MTF \times STF \quad (22)$$

As illustrated in Figure 17, the system transfer function, as degraded by wide-angle scatter from high spatial frequency microroughness, drops very quickly (at a spatial frequency of about  $\ell / \lambda f$ ) to a value of 1-TIS, then continues diminished proportionately by that amount

$$H(\hat{x}, \hat{y})_{\text{sys}} = (1-TIS)MTF \quad \text{for } \xi > \ell / \lambda f . \quad (23)$$

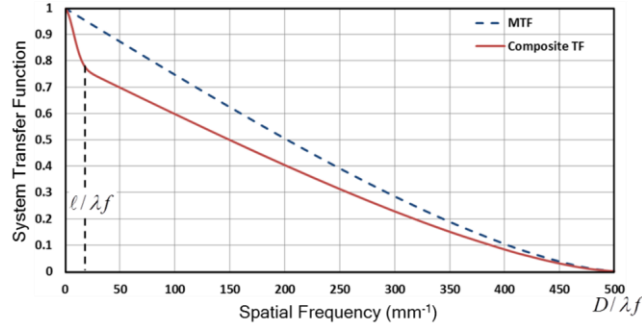


Figure 17: Illustration of the effect of surface scatter upon the MTF of an imaging system.

Reference 28 goes beyond this brief discussion of the nature of the system MTF as degraded by diffraction, geometrical aberrations, and surface scatter. It presents a parametric analysis of the effect of scattered light upon the MTF of an imaging system, and illustrates the results for three specific applications: (i) a visible Newtonian telescope with moderately good optical surfaces which produce no significant effect upon the MTF, (ii) an extreme ultraviolet Newtonian telescope where scattering effects can dominate both diffraction effects and aberrations in the resulting image degradation even for state-of-the-art optical surfaces, and (iii) a visible system made up of three diamond-turned off-axis aspheric mirrors where we use the predicted MTF to estimate whether post-polishing is required (huge cost and schedule impact) to meet a specific image quality requirement.

### 6.0 Application 1: A Systems Engineering Analysis of the Solar X-ray Imager.

As each SXI Mirror was fabricated, the metrology data was used to model the “as-manufactured” optical performance as degraded by aperture diffraction effects, geometrical aberrations, surface scatter effects, and an estimate of a variety of other miscellaneous residual errors listed in the system engineer’s error budget tree.

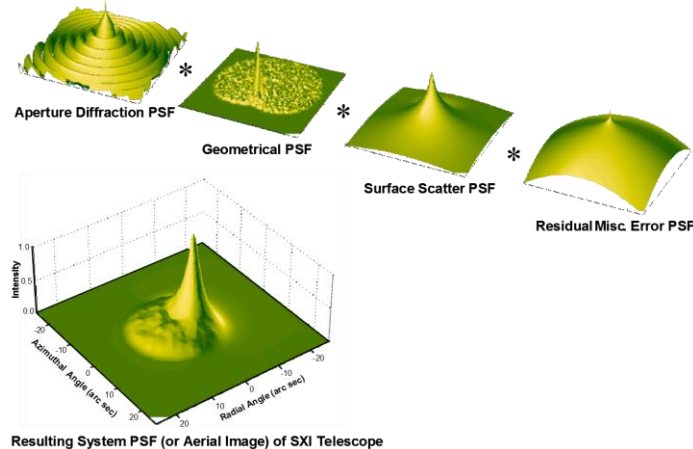


Figure 18. Schematic illustration of the individual image degradation mechanisms and the resulting convolution (*aerial image*) of the SXI telescope for a field angle of 15 arc min and a wavelength of  $44.7\text{\AA}$ .

The SXI telescope is one of the instruments on the GOES weather satellites at synchronous orbit, operating as a staring telescope recording fine detail in an extended image of the sun at wavelengths between  $6\text{\AA}$  and  $60\text{\AA}$ . Figure 19 shows: (a) the image quality predictions (half-power radius of the PSF vs field angle)

assuming geometrical aberrations only, (b) the aerial image, which includes the effects of diffraction and scattering, and (c) also includes a detailed analysis of detector effects.<sup>30</sup> The black Dots represent experimental on-orbit data taken shortly after launch. The excellent agreement between the image quality predictions and experimental data validates our image analysis method.<sup>31</sup>

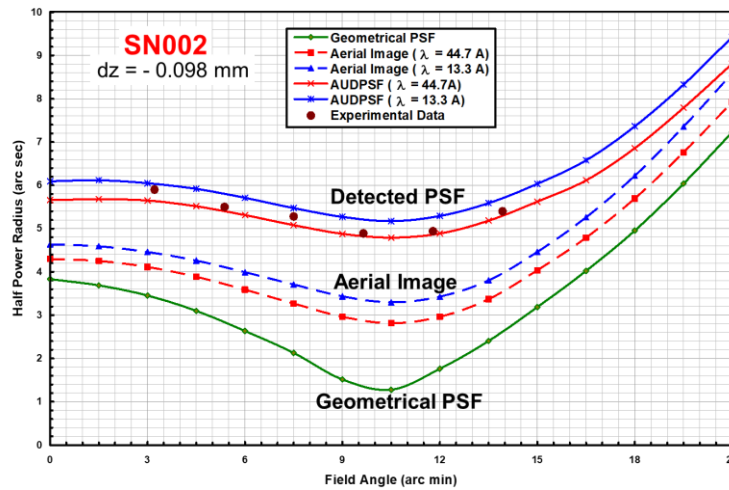


Figure 19. Image quality analysis, including detector effects, experimentally validated by on-orbit measurements after launch.

### 7.0 Application B: Integrating Fabrication and Metrology into the Optical Design Process.

With the image analysis techniques that we have demonstrated in this paper, we are now poised to fully integrate optical metrology and fabrication into the optical design process as shown schematically in Figure 20.<sup>32</sup>

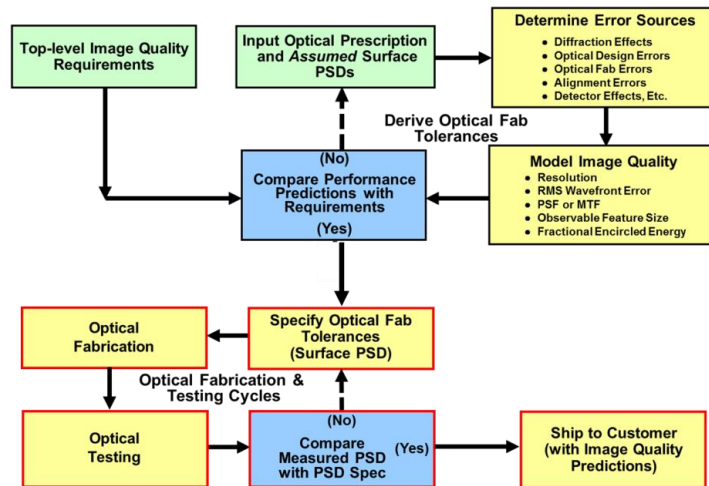


Figure 20. Flow chart indicating the strategy for integrating optical metrology and fabrication into the optical design process.

The strategy is to start with a preliminary optical design and first calculate the image quality as degraded by surface scatter effects based upon an *assumed* surface PSD. Varying this assumed surface PSD until the predicted image quality satisfies the top-level image quality requirement is a method of deriving the necessary optical fabrication tolerances. If the derived tolerances are unreasonable, the design is varied until reasonable optical fabrication tolerances are obtained. During the optical fabrication process the measured metrology data from each test cycle is compared to the derived tolerances. When they compare favorably the product is shipped to the customer along with the image quality predictions.

## References

1. J. E. Harvey, *Light-scattering Characteristics of Optical Surfaces*, Ph.D. Dissertation, University of Arizona (1976).
2. J.M.Bennett and L.Mattsson, *Introduction to Surface Roughness and Scattering*, Opt.Soc.Am., Washington D.C. (1989).
3. J. C. Stover, *Optical Scattering, Measurement and Analysis*, 2nd Edition, SPIE Press, Bellingham, WA (1995).
4. R. J. Noll, "Effect of Mid and High Spatial Frequencies on Optical Performance", *Opt. Eng.* 18, 137 (1979).
5. J. E. Harvey, E. C. Moran and W. P. Zmek, "Transfer Function Characterization of Grazing Incidence Optical Systems", in *Grazing Incidence Optics for Astronomical and Laboratory Applications*, S. Bowyer and J. Green, eds., Proc. SPIE **830-05**, 37-43 (1987).
6. D. M. Aikens, et.al., "The use of PSD Functions in Specifying Optics for the National Ignition Facility", in *OF & T*, Proc. 2576 (June 1995).
7. J. E. Harvey and A. Kotha, "Scattering Effects from Residual Optical Fabrication Errors", presented at the International Conference on Optical Fabrication and Testing, Tokyo, Japan, 5-7 June 1995; published in Proc. SPIE **2576-25**, 155-174 (1995).
8. J. E. Harvey, "Bridging the Gap between 'Figure' and 'Finish'", OSA Optical Fabrication & Testing Meeting Boston, MA (May 3, 1996).
9. D. M. Aikens, "Specification and Control of Mid-Spatial Frequency Wavefront Errors in Optical systems", OSA Topical Meeting on Optical Fabrication and Testing, Rochester, NY (2008).
10. Paul Murphy, "Methods and Challenges in Quantifying Mid-Spatial Frequencies", OSA Topical Meeting on Optical Fabrication and Testing, Rochester, NY (2008).
11. Angela Duparre, "Characterization of Surface and Thin-Film Roughness using PSD Functions", OSA Topical Meeting on Optical Fabrication and Testing, Rochester, NY (2008).
12. P. Glenn, P. Reid, A. Slomba, and L. P. Van Speybroeck, "Performance Prediction of the AXAF Technology Mirror Assembly using measured Mirror Errors", *Appl. Opt.* 27,1639 (1988).
13. E. L Church, et. al., "Relationship between Surface Scattering and Microtopographic Features", *Opt. Eng.* **18** (2) 1979.
14. D. P. Gaines, et. al., "Surface Characteristics of Optics for EUV Lithography", OSA Topical Meeting, Boston, MA (May 1996).
15. D. Martinez-Galarce, J. E. Harvey, M. Bruner, J. Lemen, E. Gullikson, R. Soufli, E. Prast and S. Khatri, "A Novel Forward-model Technique for Estimating EUV Imaging Performance: Design and Analysis of the SUVI Telescope", Proc. SPIE **7732-177** (July 2010).
16. E. L. Church and P. Z. Takacs, "The optimal estimation of finish parameters", Proc. SPIE 1530, p. 71-78 (1991).
17. J. E. Harvey, S. Schroder, N. Choi, and A. Duparre, "Total integrated scatter from surfaces with arbitrary roughness, correlation widths, and incident angles", *Opt. Eng.* **51**(1), (Jan 2012).
18. A. Krywonos, J. E. Harvey and N. Choi, "Linear systems formulation of surface scatter theory for rough surfaces with arbitrary incident and scattering angles", *J. Opt. Soc. Am. A* **28**(6) 1121-1138 (June 2011).
19. J. E. Harvey, *Understanding Surface Scatter Phenomena; A Linear Systems Theory Formulation*, SPIE Press (2019).
20. J. A. Ratchiff, "Some Aspects of Diffraction Theory and Their Application to the Ionosphere", in *Reports of Progress in Physics*, edited by A. C. Strickland (The Physical Society, London, 1956), Vol. XIX.
21. J. W. Goodman, *Introduction to Fourier Optics*, 2nd Ed., McGraw-Hill, New York (1996).
22. J. D. Gaskill, *Linear Systems, Fourier Transforms, and Optics*, Wiley, New York (1978).
23. A. J. S. Hamilton, "Uncorrelated modes of nonlinear power spectrum," *Monthly Notices of the Royal Astronomical Society* **312**(2), 257-284 (2000).
24. N. Choi and J. E. Harvey, "Numerical validation of the Generalized Harvey-Shack surface scatter theory", *Opt. Eng.* **52**(11), 115103 (November 26, 2013); doi: 10.1117/1.OE.52.11.115103.
25. J. E. Harvey, Narak Choi, Andrey Krywonos and Jesus Marcen, "Calculating BRDFs from Surface PSDs for Moderately Rough Surfaces", Presented at SPIE's International Symposium on Optics and Photonics, San Diego, CA (Aug 2009); published in Proc. SPIE **7426-42** (August 2009).
26. J. E. Harvey, N. Choi, A. Krywonos, G. Peterson, and M. Bruner, "Image Degradation due to Scattering Effects in Two-mirror Telescopes", *Opt. Eng.* Vol **49**(6), (June 2010).
27. Gary Peterson, "Analytic Expressions for In-field Scattered Light Distribution", Proc SPIE 5178-01, 184-193 (2004).
28. J. E. Harvey, "Parametric analysis of the effect of scattered light upon the modulation transfer function", *Opt. Eng.* **52**(7), (July 2013).
29. V. N. Mahajan, *Optical Imaging and Aberrations: Part II Wave Diffraction Optics*, SPIE Press, Bellingham, WA (2001), pp 96.
30. J. E. Harvey, Martina Atanassova, and A. Krywonos, "Balancing detector effects with aberrations in the design of wide-field grazing incidence x-ray telescopes", *Opt. Eng.* **45** (6), Art. No. 063003, 1-10 (June 2006).
31. J. E. Harvey, A. Krywonos, M. Atanassova, and P.L. Thompson, "The Solar X-ray Imager (SXI) on GOES-13: Design, Analysis, and On-orbit Performance", Proc. SPIE **6689**, 668901-1 to 668901-9 (August 2007).
32. J. E. Harvey, "Integrating optical fabrication and metrology into the optical design process", *Appl. Opt.* **54**, 2224-2233 (2015).